

Searches for invisibly decaying Higgs bosons with the CMS detector

Patrick James Dunne
of Imperial College London

A dissertation submitted to Imperial College London
for the degree of Doctor of Philosophy

Abstract

Declaration

This dissertation is the result of my own work, except where explicit reference is made to the work of others, and has not been submitted for another qualification to this or any other university. This dissertation does not exceed the word limit for the respective Degree Committee.

Patrick Dunne

Acknowledgements

Contents

1	Introduction and theory	2
1.1	The standard model of particle physics	2
1.1.1	Fundamental particles in nature	3
1.1.2	Introduction to gauge theories	4
1.2	The SM gauge group and fundamental particle representations	6
1.2.1	Spontaneous symmetry breaking and the Higgs mechanism	8
1.2.2	Higgs boson production and decay at the LHC	9
1.2.3	Challenges for the SM	9
1.3	Dark matter	9
1.4	Some extensions of the standard model incorporating dark matter	9
1.5	Simulation	9
2	The LHC and the CMS experiment	10
2.1	The LHC	10
2.2	The CMS experiment	16
2.2.1	Tracker	18
2.2.2	Electromagnetic calorimeter	19
2.2.3	Hadronic calorimeter	21
2.2.4	Muon system	22
2.2.5	Trigger system and data processing	24
3	Physics objects and event reconstruction	27
3.1	Tracks	27
3.2	Primary vertex	28
3.3	Particle Flow	29
3.4	Electrons	30
3.5	Muons	32
3.6	Jets	33
3.6.1	Jet clustering	33

3.6.2	Jet identification	34
3.6.3	Jet energy corrections	35
3.7	Missing transverse energy	36
3.8	Taus	38
4	Methods for limit setting	39
5	Search for invisibly decaying Higgs bosons in Run 1 prompt data	40
5.1	Trigger and event selection	40
5.2	Background estimation	40
5.2.1	$W \rightarrow e\nu + \text{jets}$	40
5.2.2	$W \rightarrow \mu\nu + \text{jets}$	40
5.2.3	$W \rightarrow \tau\nu + \text{jets}$	40
5.2.4	$Z \rightarrow \nu\nu + \text{jets}$	40
5.2.5	QCD	40
5.2.6	Minor backgrounds	40
5.3	Systematic uncertainties	40
5.4	Results	40
6	Search for invisibly decaying Higgs bosons in Run 1 parked data	41
6.1	Trigger	42
6.2	Event selection	42
6.3	Background estimation	42
6.3.1	$W \rightarrow e\nu + \text{jets}$	42
6.3.2	$W \rightarrow \mu\nu + \text{jets}$	42
6.3.3	$W \rightarrow \tau\nu + \text{jets}$	42
6.3.4	$Z \rightarrow \nu\nu + \text{jets}$	42
6.3.5	QCD	42
6.3.6	Minor backgrounds	42
6.4	Systematic uncertainties	42
6.5	Results	42
7	Combinations and interpretations of Run 1 searches for invisibly decaying Higgs bosons	43
7.1	Searches in other channels	43
7.2	Combination with prompt VBF search	43
7.3	Combination with the parked VBF search	43

Contents 1

7.4	Dark matter interpretations	43
8	Search for invisibly decaying Higgs bosons in Run 2 data	44
	Bibliography	46
	List of figures	50
	List of tables	51
	Acronyms	52

Chapter 1

Introduction and theory

This chapter will explain the theory of invisible decays of the Higgs boson (“Higgs to invisible”). It will start with an introduction to the standard model (SM), focussing on the Higgs mechanism, before outlining the motivations behind and some candidates for physics beyond the SM (BSM). Natural units, where $\hbar = c = 1$, Einstein summation convention and Feynman slash notation are used throughout. Four vector indices are labelled using greek letters, and gauge group generators using roman letters.

1.1 The standard model of particle physics

The SM describes the interaction of the particles currently thought to be fundamental with the strong, weak and electromagnetic forces. Its predictions, which come from specifying the symmetries the theory respects and how they are broken, the particles in the theory, and 18 free parameters, have been tested in many different experiments, in some cases up to one part in a trillion [1]. However, it does face challenges, described in section Section 1.2.3, one example being that it does not describe dark matter (DM).

The SM is a gauge invariant quantum field theory (QFT). To construct a QFT the symmetries that are respected by the theory and the fields it describes must be specified. The symmetries are important because of Noether’s theorem, which states that for every continuously differentiable symmetry of the Lagrangian of a theory there is a corresponding conservation law [2,3]. An example of this is Poincaré invariance, the invariance of the laws of physics under translations and rotations in space and time, which leads through Noether’s theorem to the conservation of energy, linear momentum and angular momentum. In addition to giving rise to conservation laws, some types of

Table 1.1: The fundamental fermions observed in nature separated into their three generations. Each particle shown also has an antiparticle with opposite charge and identical mass. Values taken from [5]

Generation	Leptons			Hadrons		
	Particle	Mass	Charge	Particle	Mass	Charge
1	e^-	511 keV	-1	u	2.3 MeV	$+\frac{2}{3}$
	ν_e	~ 0	0	d	4.8 MeV	$-\frac{1}{3}$
2	μ^-	105.7 MeV	-1	c	1.275 GeV	$+\frac{2}{3}$
	ν_μ	~ 0	0	s	95 MeV	$-\frac{1}{3}$
3	τ^-	1.777 GeV	-1	t	173.2 GeV	$+\frac{2}{3}$
	ν_τ	~ 0	0	b	4.18 GeV	$-\frac{1}{3}$

symmetry lead to additional fields being required to preserve invariance, this will be discussed further in Section 1.1.2 [4].

It is important to specify the fields described by the QFT as these are constrained by the fundamental particles seen in nature. This is because particles correspond to the quantised excitations of fields. Specifically, scalar fields correspond to spin zero bosons, spinor fields correspond to spin half fermions, and vector fields correspond to spin 1 bosons. In order to add a new field an explanation for why the corresponding particle has not yet been observed must, therefore, be provided. We will now go through the particles observed in nature and how they are represented in the SM.

1.1.1 Fundamental particles in nature

There are two types of fundamental particles in nature, fermions and bosons. The fermions observed in nature that are currently thought to be fundamental are then divided into those which interact via the strong nuclear force (the quarks), and those which don't (the leptons). Both the quarks and leptons have two further types: charged and neutral in the case of the leptons, and up type and down type in the case of the fermions. Another interesting feature of the fermions is that they are arranged in three generations. Each generation has one fermion of each type with the same quantum numbers as those in the other generations, except that the mass is different. Table 1.1 shows this structure.

Table 1.2: The fundamental vector bosons observed in nature separated by the force which they mediate. Values taken from [5].

Force	Particle	Mass	Charge
Electromagnetism	γ	0	0
Weak	W^\pm	80.4 GeV	± 1
	Z	91.2 GeV	0
Strong	g	0	0

The bosons in nature also have two types. The first type are vector bosons which mediate the three fundamental interactions described by the SM. The vector bosons are summarised in Table 1.2, where it can be seen that their masses are very different, the photon and the eight gluons being massless, while the W^\pm and Z bosons are very massive. As we will see in Section 1.2.1 explaining these masses requires the Higgs mechanism. The Higgs mechanism also gives rise to the other type of boson seen in nature, the scalar Higgs boson. In order to see how all of the above particles are represented in the SM an introduction to gauge theories is necessary.

1.1.2 Introduction to gauge theories

Gauge symmetries are local transformations, i.e. the transformation can be different at different points in space and time, that form a symmetry group. To see the effect of imposing such a symmetry on a theory consider imposing local invariance under U(1) transformations on the Dirac Lagrangian for a massive fermion:

$$\mathcal{L} = i\bar{\psi}\not{\partial}\psi - m\bar{\psi}\psi \quad [6]. \quad (1.1)$$

This Lagrangian is invariant under a global $U(1)$ transformation $\psi \rightarrow e^{iq\theta}\psi$, where q and θ are constant. However, if the $U(1)$ transformation is local i.e. θ is a function of spacetime position the Lagrangian is no longer invariant and transforms as:

$$\mathcal{L} \rightarrow \mathcal{L} - q(\partial_\mu\theta)\bar{\psi}\gamma^\mu\psi. \quad (1.2)$$

In order to restore invariance a vector field, A_μ , referred to as a gauge field or gauge boson, which transforms as $A_\mu \rightarrow A_\mu + \partial_\mu \theta$ and has an interaction with the fermion field:

$$\mathcal{L}_{int} = q(\bar{\psi}\gamma^\mu\psi)A_\mu, \quad (1.3)$$

can be added to the theory. The interaction term of the new gauge field transforms as:

$$\mathcal{L}_{int} \rightarrow \mathcal{L}_{int} + q(\partial_\mu\theta)\bar{\psi}\gamma^\mu\psi, \quad (1.4)$$

which cancels out the non-gauge invariance seen in equation (1.2).

Assuming the new gauge field to be massless the Lagrangian is now:

$$\mathcal{L} = i\bar{\psi}\not{\partial}\psi - m\bar{\psi}\psi + q(\bar{\psi}\gamma^\mu\psi)A_\mu - \frac{1}{4}F_{\mu\nu}F^{\mu\nu}, \quad (1.5)$$

where $F_{\mu\nu}$ is the field strength tensor of the vector field. For a gauge boson from a general gauge group is written as:

$$F_{\mu\nu}^a = \partial_\mu A_\nu^a - \partial_\nu A_\mu^a + g f^{abc} A_\mu^b A_\nu^c, \quad (1.6)$$

where f^{abc} are the structure constants of the gauge group, which are a representation of the comutation relations between the group's generators. For $U(1)$ which only has one self-commuting generator the single structure constant is 0. However, for non-Abelian gauge groups (i.e. those with non-commuting generators) they can be non-zero causing the $F_{\mu\nu}F^{\mu\nu}$ term in the Lagrangian to include self-interaction terms of the vector bosons.

It is also interesting to note that equation (1.5) can be rewritten as:

$$\mathcal{L} = i\bar{\psi}\gamma^\mu\mathcal{D}_\mu\psi - m\bar{\psi}\psi - \frac{1}{4}F_{\mu\nu}F^{\mu\nu}, \quad (1.7)$$

where $\mathcal{D}_\mu = \partial_\mu + iqA_\mu$ and is referred to as the covariant derivative. Comparing equation (1.1) and equation (1.7) it can be seen that to go from a globally invariant Lagrangian to a locally invariant one we have substituted the normal spacetime derivative for the covariant derivative and added the free term of the vector field.

$U(1)$ transformations have one degree of freedom and can be described by one parameter, in the above case θ , and in order to make the Lagrangian locally invariant one interacting gauge boson had to be added. This correspondence between the number of degrees of freedom and the number of gauge bosons holds generally. For each degree of freedom of

a group's transformations there exists a generator of the group, and for each generator one interacting gauge boson must be added to achieve local invariance.

1.2 The SM gauge group and fundamental particle representations

The SM is gauge invariant under the group $SU(3)_C \otimes SU(2)_L \otimes U(1)_Y$. Fermions in the SM are spin half spinor representations of these symmetry groups. These spinors can be split into chirally left and right handed components using the projection operators $P_L = \frac{1}{2}(1 \mp \gamma^5)$. Chirally left and right handed fermions transform differently under $SU(2)_L$. The right handed spinors are not charged under $SU(2)_L$ and thus are represented as a singlet, while the left handed spinors transform as a doublet.

The first generation of leptons can, therefore, be written as:

$$\psi_1 = e_R, \psi_2 = L = \begin{pmatrix} \nu_e \\ e_L \end{pmatrix}. \quad (1.8)$$

The SM treats neutrinos as massless and has no right handed neutrino. Similarly the first generation of quarks can be written as:

$$\psi_3 = u_R, \psi_4 = d_R, \psi_5 = \begin{pmatrix} u_L \\ d_L \end{pmatrix}. \quad (1.9)$$

As we saw in Section 1.1.2 gauge symmetries in theories with fermions require the addition of an interacting vector boson per symmetry generator to preserve gauge invariance. $SU(3)_C$ has eight generators whose eight vector bosons, $G_{a\mu}$, correspond to the eight physical gluons which mediate the strong interaction. $SU(2)_L$ has three generators whose three vector bosons, W_μ^i , mix with the one vector boson from $U(1)_Y$, B_μ unifying the electromagnetic and weak forces into one electroweak force. The physical states that

result are:

$$\begin{aligned} W^\pm_\mu &= \frac{1}{\sqrt{2}} (W^1_\mu \mp i W^2_\mu) \\ Z_\mu &= \cos(\theta_W) W^3_\mu - \sin(\theta_W) B_\mu \\ A_\mu &= \sin(\theta_W) W^3_\mu + \cos(\theta_W) B_\mu, \end{aligned} \tag{1.10}$$

where θ_W is the Weinberg angle and A_μ is the photon field. Also, as described in Section 1.1.2 the interaction between these vector bosons and the fermion fields occurs through their presence in the covariant derivative, and interactions between the vector bosons occur because $SU(3)_C$ and $SU(2)_L$ are non-Abelian.

Now let us try to construct a Lagrangian for these fields. First ignoring the masses we find:

$$\mathcal{L} = i\bar{\psi}_i \not{\mathcal{D}} \psi_i - \frac{1}{4} F_{\mu\nu j} F_j^{\mu\nu}, \tag{1.11}$$

where the sum over all ψ also includes the second and third generations, $F_{\mu\nu j} F_j^{\mu\nu}$ is a sum of the free terms of all the SM gauge bosons and $\not{\mathcal{D}}$ is the SM covariant derivative:

$$\mathcal{D}_\mu = \partial_\mu + ig_1 \frac{Y}{2} B_\mu + ig_2 \frac{\tau_i}{2} W_\mu^i + ig_3 \frac{\lambda_a}{2} G_\mu^a, \tag{1.12}$$

with Y being the constant generator of $U(1)$, τ_i the generators of $SU(2)_L$, λ_a the generators of $SU(3)_C$ and g_i the coupling constants of the fields. It should be noted that $\frac{g_1}{g_2}$ is equal to $\tan(\theta_W)$.

When we try to include mass a problem occurs. We know that some of the fermions have mass, and consequently we should have fermion mass terms of the form:

$$\begin{aligned} \mathcal{L}_{m_f} &= -m_f \bar{f} f \\ &= -m_f \bar{f} \left[\frac{1}{2} (1 - \gamma^5) + \frac{1}{2} (1 + \gamma^5) \right] f \\ &= -m_f (\bar{f}_R f_L + \bar{f}_L f_R), \end{aligned} \tag{1.13}$$

in our Lagrangian. However, as the left and right handed fields do not transform in the same way under $SU(2)_L$ this term breaks the gauge symmetry of the Lagrangian and can't be present.

A similar problem occurs for vector fields. In Section 1.1.2 we didn't consider the mass term of these vector fields:

$$\mathcal{L}_{m_V} = \frac{1}{2} m_V^2 A_\mu A^\mu, \quad (1.14)$$

which is not gauge invariant, so massive vector bosons are not possible on their own in gauge invariant theories either. The additional piece of the SM required to allow particles to have mass is the Higgs mechanism.

1.2.1 Spontaneous symmetry breaking and the Higgs mechanism

The Higgs mechanism is a form of spontaneous symmetry breaking. A symmetry is said to be spontaneously broken when the Lagrangian remains invariant while the vacuum state, i.e. that with lowest energy, does not. Terms which are not gauge invariant can then be incorporated into the theory by adding a field which has a non-zero vacuum expectation value and coupling it to the other fields present in the term. For the Higgs mechanism this field is a complex scalar $SU(2)_L$ doublet, called the Higgs field:

$$\phi = \begin{pmatrix} \phi^+ \\ \phi^0 \end{pmatrix}. \quad (1.15)$$

The main part of the Higgs field Lagrangian is:

$$\mathcal{L} = T - V = (\mathcal{D}_\mu \phi)^\dagger (\mathcal{D}^\mu \phi) + \mu^2 \phi^\dagger \phi - \lambda (\phi^\dagger \phi)^2. \quad (1.16)$$

For $\mu^2 > 0$ the minima of the potential are non-zero and form a circle in phase space of ϕ . All of these vacua are equivalent and a particular vacuum can be chosen with no physical effect. By convention we choose the following vacuum:

$$\langle 0 | \phi | 0 \rangle = \begin{pmatrix} 0 \\ \sqrt{\frac{\mu^2}{2\lambda}} \end{pmatrix} = \frac{1}{\sqrt{2}} \begin{pmatrix} 0 \\ v \end{pmatrix}. \quad (1.17)$$

Next we consider small perturbations around this vacuum, ignoring those that can be set to zero by gauge freedom gives:

$$\phi = \begin{pmatrix} 0 \\ v + H \end{pmatrix}. \quad (1.18)$$

Inserting this into equation (1.16) and ignoring terms with more than one type of field gives at leading order:

$$\mathcal{L} = \frac{1}{2}\partial_\mu H\partial^\mu H - \frac{1}{2}\mu^2 H^2 + \frac{v^2}{8} [g_2^2 W_\mu^+ W^{+\mu} + g_2^2 W_\mu^- W^{-\mu} + (g_1^2 + g_2^2) Z_\mu Z^\mu]. \quad (1.19)$$

As expected, the weak vector bosons W_μ^\pm and Z_μ acquire masses $\frac{gv}{2}$ and $\frac{v}{2}\sqrt{g_1^2 + g_2^2}$ respectively. We also see an additional massive scalar H , which is the Higgs boson, which has mass $\sqrt{2}\mu$. The photon and gluons do not acquire masses as the particular choice of coupling constants and the structure of the group generators leads to the terms in A_μ and $G_{\mu a}$ being zero.

The final part of the Higgs field Lagrangian is that giving rise to the fermion masses. These are generated by a Yukawa term in the Lagrangian for each fermion as follows:

$$\mathcal{L}_{Yuk} = k_f (\bar{f}_L \phi f_R + \bar{f}_R \phi^\dagger f_L). \quad (1.20)$$

The fermion's mass is then $\frac{k_f v}{\sqrt{2}}$.

1.2.2 Higgs boson production and decay at the LHC

1.2.3 Challenges for the SM

1.3 Dark matter

1.4 Some extensions of the standard model incorporating dark matter

1.5 Simulation

Chapter 2

The LHC and the CMS experiment

This chapter introduces the CMS [7] experiment and the LHC [8]. In Section 2.1 an overview of the LHC and the chain of accelerators which feed into it is given. This is then followed in Section 2.2 by a description of the CMS experiment focussing on the aspects most relevant to the search for invisibly decaying Higgs bosons.

2.1 The LHC

The LHC is situated 100m underground in a tunnel formerly built for the LEP accelerator [9] at CERN near Geneva, Switzerland. It is a 27km storage ring which accelerates both protons and heavy ions and collides them at the highest centre of mass energies of any collider built to date. The work contained in this thesis uses data from proton-proton collisions (“events”). These protons are obtained by taking hydrogen gas and stripping its atoms of their electrons with an electric field. The first accelerator in the chain of accelerators feeding into the LHC, Linac 2, accelerates the protons to 50 MeV. The protons are then accelerated to 1.4 GeV by the next accelerator, the Proton Synchrotron Booster (PSB), which is followed by the Proton Synchrotron (PS) where they reach 25 GeV. The beam energy is then increased to 450 GeV in the Super Proton Synchrotron (SPS). Finally, the protons are injected into the LHC where, at time of writing, the maximum energy the beams have been accelerated to is 6.5 TeV, close to the design maximum of 7 TeV.

When fully filled the LHC contains two counter-rotating beams which are formed of up to 2808 bunches spaced either 25 or 50 ns apart and each containing $\mathcal{O}(10^{11})$ protons. The two beams are kept travelling in a circle by 1232 superconducting dipole magnets

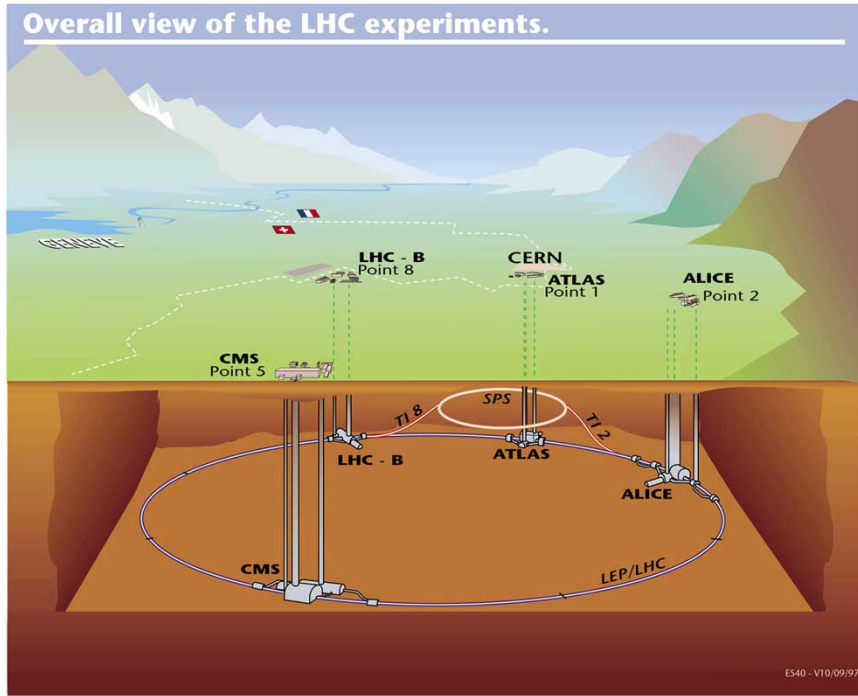


Figure 2.1: The layout of the chain of accelerators feeding into the LHC, showing the position of the four main detectors.

and steered to four collision points around the LHC. Detectors are situated at these collision points to observe the interactions, the main four being: ALICE [10], ATLAS [11], CMS [7] and LHCb [12]. A schematic of the chain of accelerators feeding into the LHC and the LHC detectors can be seen in Figure 2.1.

When studying a physical process occurring in particle collisions it is important to know how many times it will occur, this can be expressed as:

$$N = \mathcal{L}\sigma, \quad (2.1)$$

where \mathcal{L} , the integrated luminosity, depends only on the parameters of the collisions, and the cross-section, σ , depends only on the process. In order to observe rare (i.e. low cross-section) processes, such as those studied at the LHC, it is, necessary to use very high luminosity datasets. The integrated luminosity is obtained by integrating the instantaneous luminosity over time, so large luminosities can be obtained either by running the accelerator for a long time, or by operating at high instantaneous luminosity.

For collisions at the LHC the instantaneous luminosity is given by:

$$\mathcal{L} = \frac{k_b N_b^2 f_{rev} \gamma}{4\pi \epsilon_n \beta} [13], \quad (2.2)$$

where k_b is the number of bunches per beam, N_b the number of protons per bunch, f_{rev} the revolution frequency, ϵ_n the normalised transverse beam emittance, β^* the beta-function at the interaction point and γ the Lorentz factor. The design instantaneous luminosity of the LHC is $10^{34} \text{ cm}^{-2}\text{s}^{-1}$ with 25ns bunch spacing. The integrated luminosity is defined as $\mathcal{L}_{int} = \int \mathcal{L} dt$.

The LHC started physics runs in 2010, during which it operated at a centre of mass energy of 7 TeV and delivered an integrated luminosity of 44.2 pb^{-1} to CMS. In 2011 the LHC also operated at 7 TeV and delivered 6.1 fb^{-1} to CMS. The centre of mass energy was increased to 8 TeV in 2012 and 23.3 fb^{-1} of data were delivered to CMS. A summary of the luminosity delivered to CMS during the three periods of Run 1 can be seen in Figure 2.2. In Run 2 the centre of mass energy was further increased to 13 TeV and during 2015 4.09 fb^{-1} of data were delivered to CMS at this energy. In order to be used for physics analysis data must be certified. This certification ensures that the detector was fully operational when the data were recorded. In 2011 5.1 fb^{-1} were certified, in 2012 19.7 fb^{-1} were certified and in 2015 2.2 fb^{-1} were certified.

The cross-sections for several processes are shown in Figure 2.3 and it can be seen that the cross-section for VBF Higgs production is approximately 1.5 pb. Therefore, we expect approximately 30000 VBF produced Higgs bosons in the 2012 dataset. By contrast the vector boson production cross-section is approximately 100 nb and the total cross-section for any process is orders of magnitude higher still. The separation of the relatively small number of signal events from the large background is a major challenge for the search for invisibly decaying Higgs bosons.

The large total cross-section combined with the high instantaneous luminosities that the LHC operates at leads to the probability for multiple proton-proton interactions per bunch crossing being high. The distribution of the number of interactions per bunch crossing can be seen in Figure 2.4. The additional interactions on top of the process of interest in a bunch crossing are called pile-up (PU).

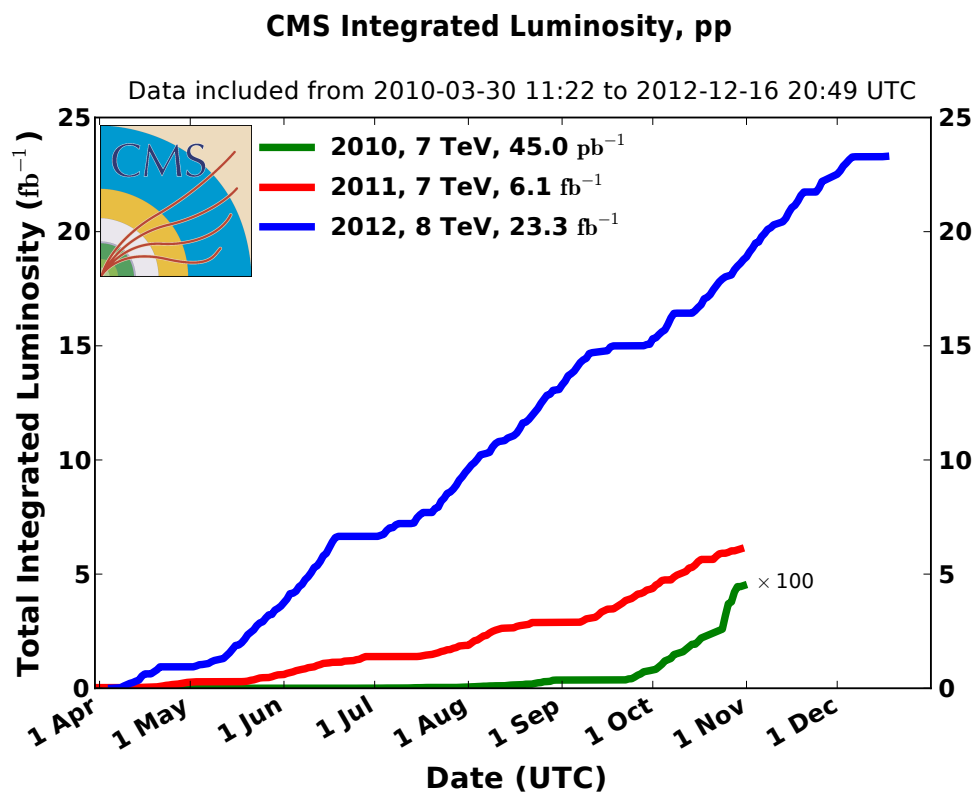


Figure 2.2: A summary of the luminosity delivered to CMS during Run 1 of the LHC [14].

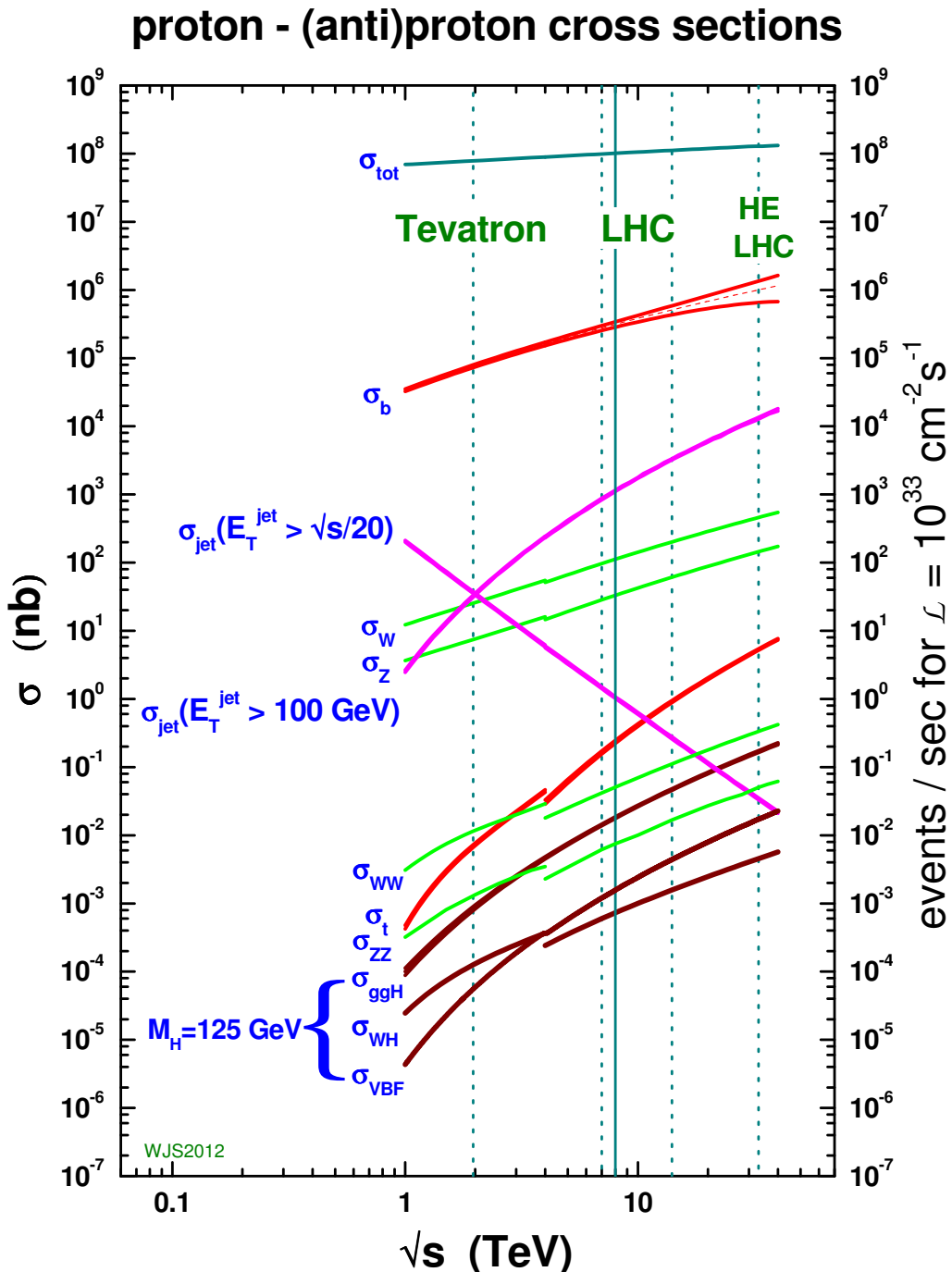


Figure 2.3: Cross-sections for several processes in collisions of protons with protons or anti-protons as a function of centre of mass energy. The energies that the LHC and Tevatron ran at are highlighted [15].

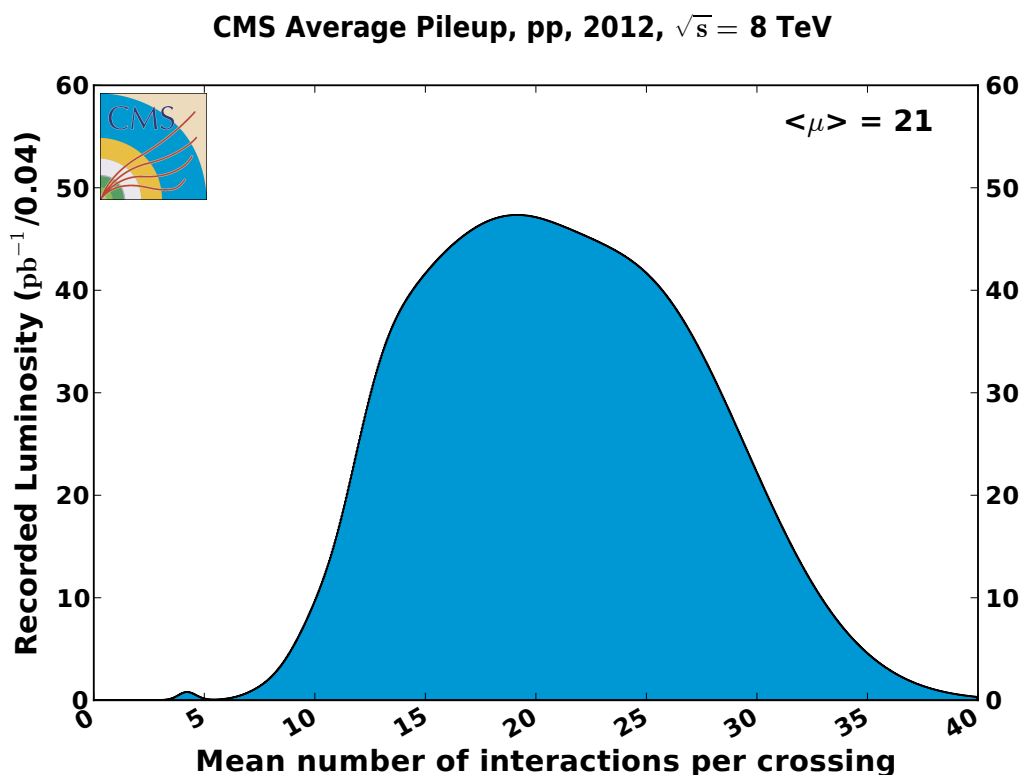


Figure 2.4: Distribution of the number of interactions per bunch crossing in CMS during 2012 running of the LHC [14].

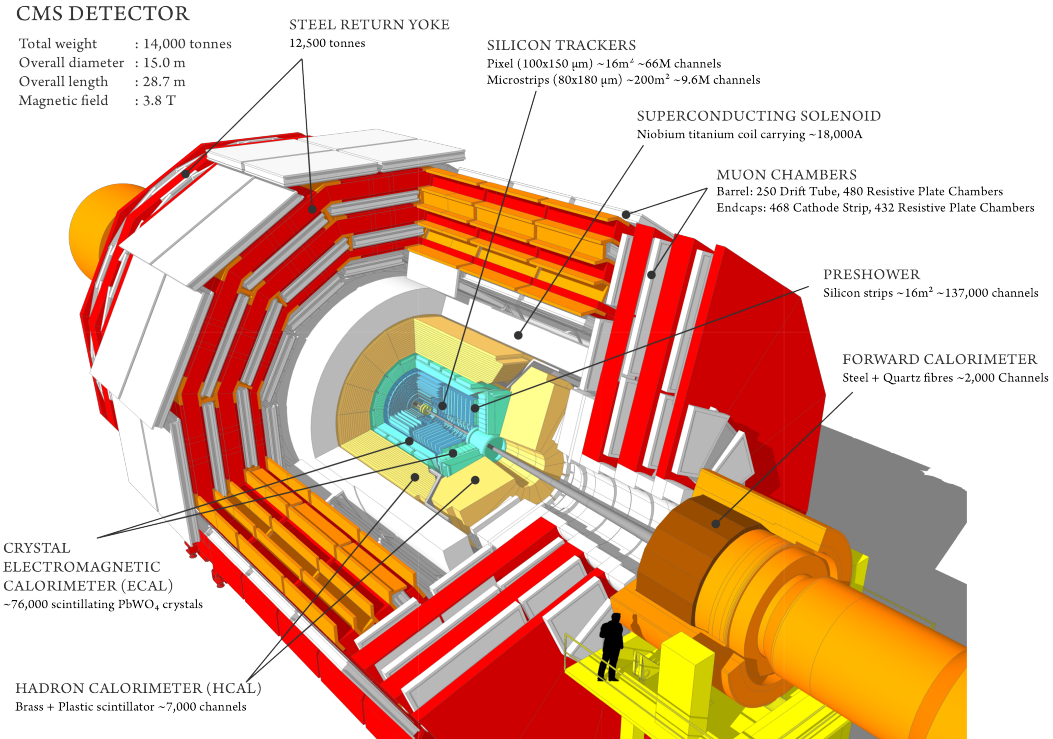


Figure 2.5: A diagram of the subsystems making up the CMS detector, illustrating the hermeticity and layered structure of the experiment [16].

2.2 The CMS experiment

The CMS detector was designed to search for the SM Higgs and new physics at the TeV energy scale. Both because the nature of new physics is not known and the SM Higgs has a wide range of decays and production mechanisms CMS must be sensitive to many different types of final state particles and topologies. In order to achieve this it has a hermetic design comprising a barrel, endcaps and a forward calorimetry system, and is also composed of several layers of subdetectors each sensitive to different particles as shown in Figure 2.5. The hermeticity of the detector is particularly important for the VBF Higgs to invisible search, because, as described in Section 1.2.2, the VBF final state is highly likely to have jets in the forward regions of the detector. Further details on the CMS detector beyond those in this section can be found in Ref. [7].

A central design feature of CMS is the superconducting magnet, inside which is generated a 3.8T axial field. This field bends the path of charged particles travelling through it allowing their momentum to be measured. Not all particles are charged however, and the path of several types of particles through the CMS detector is shown in Figure 2.6. The first layer is the tracker which records the paths taken by charged particles, as well

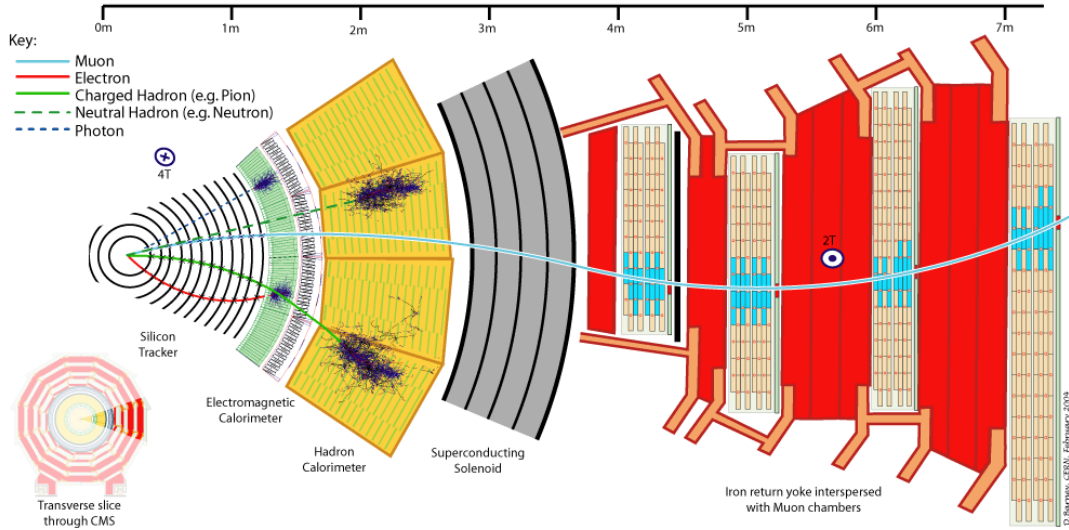


Figure 2.6: A schematic cross-section of the CMS experiment showing the path taken by several types of particles [17].

as providing a momentum measurement the tracks also allow the vertex from which the particle came to be identified. The next layer is the electromagnetic calorimeter (ECAL) where electrons and photons deposit energy through electromagnetic showers. This is followed by the hadron calorimeter (HCAL) where hadrons deposit most of their energy. After the calorimetry systems is the superconducting magnet which is not instrumented. Outside the magnet are the muon detection systems, which are interspersed with iron plates which form the return yoke for the magnet. Due to their high mass compared to electrons, muons do not deposit much energy in the detector and often are not stopped, so the muon system is primarily a tracking detector.

The origin of the co-ordinate system used by CMS is at the nominal interaction point. It is a right handed cartesian system with the x axis pointing towards the centre of the LHC ring and the y-axis vertically upwards, the z axis then points along the beam line. The azimuthal angle ϕ and the polar angle θ are measured from the x and z axes respectively. It is common to describe the direction of outgoing particles using ϕ and their pseudo-rapidity, η which is defined as:

$$\eta = -\ln[\tan(\theta/2)]. \quad (2.3)$$

Distances in the $\eta - \phi$ plane are given by $\Delta R = \sqrt{\Delta\phi^2 + \Delta\eta^2}$. Two other quantities often used at hadron colliders are the projections of a particle's momentum and energy in the transverse plane, these are denoted p_T and E_T respectively. The missing transverse

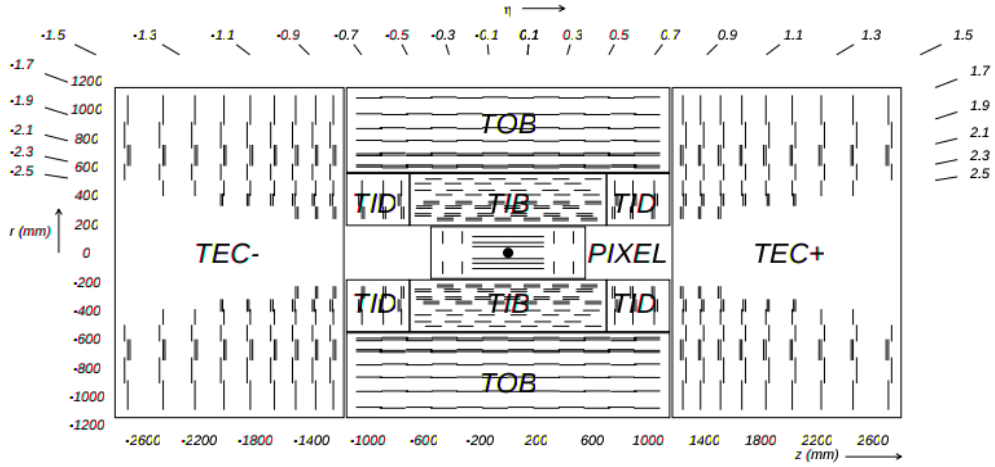


Figure 2.7: A cross-section of the CMS tracker, indicating the subsystems that comprise it. Each line indicates a detector module [7].

energy, defined as the negative vector sum of the momentum of all particles in an event, is important in inferring the presence of invisible particles and is denoted \cancel{E}_T

2.2.1 Tracker

The tracker is designed to precisely measure the paths of charged particles from LHC collisions which curve in CMS's magnetic field. The design transverse momentum resolution of the full tracking detector is 1-2% at 100GeV. In order to precisely measure the particles' positions and ensure the occupancy of the tracker is low a high granularity is required. Due to the frequency of collisions at the LHC and the high instantaneous luminosity a radiation hard system with fast response is also necessary. This combination of requirements motivates the use of a silicon based system. When traversing silicon charged particles create electron-hole pairs, which are then separated by an applied electric field, causing a current pulse.

The tracker layout can be seen in Figure 2.7. In order to keep the sensor occupancy below 1% at design luminosity, the innermost component is a silicon pixel detector. This detector has three layers in the barrel, at radii of 4.7, 7.3 and 10.2 cm, and two in the endcap. Each pixel is 100 μm x 150 μm in size and in total there are 66 million of them. The resulting resolution of the pixel detector is approximately 10 μm in the $r - \phi$ plane and 17 μm in the $r - z$ plane [18]. During run 1 the proportion of modules in the pixel (strip) tracker known to be defective was 2.4% (2.3%) [].

Surrounding the pixel detector is a silicon strip detector with 10 layers in the barrel, at radii of 20 to 116 cm, and 12 pairs of disks in the endcap. The strips are typically 10-20 cm long and 80-180 μm wide, with the strip size increasing with radius as the particle flux decreases. The strip detector's single point resolution is 230-530 μm in the $r - z$ plane and 23-52 μm in the $r - \phi$ plane. The better resolution in the $r - \phi$ plane allows a better measurement of p_T , as this is the direction in which a particle's track bends in the CMS magnetic field. The barrel and endcap detectors together have an acceptance of $|\eta| < 2.5$ for both the pixel and strip detectors. Further details on the position resolution of the tracking detector for vertex reconstruction will be given in Section 3.2.

2.2.2 Electromagnetic calorimeter

The ECAL is designed to provide accurate photon and electron reconstruction and precise measurement of the electromagnetic component of hadron jets. It is a homogeneous calorimeter made of lead tungstate (PbWO_4) crystals, separated into a barrel (ECAL barrel (EB)) section, with 61200 crystals and two endcaps (ECAL endcap (EE)) each with 7234 crystals. These crystals are 25.8 radiation lengths in depth in the barrel and instrumented with photodetectors, avalanche photodiodes being used in the barrel and vacuum phototriodes in the endcap.

The layout of the ECAL is shown in Figure 2.8. The EB crystals have a 170x360 arrangement in $\eta - \phi$ space such that the gaps between crystals are offset by 3° from the vector to the detector origin, thus avoiding particles travelling through the gaps. The EB extends to $|\eta| = 1.479$, with higher values of η covered by the EE. The crystals in the EE are arranged in an $x - y$ grid pointing at a focus 1.3m from the nominal interaction point, giving a $2 - 8^\circ$ separation between the gaps between crystals and the vector to the detector origin. In addition to the main PbWO_4 detector the endcaps also have a preshower detector. This preshower is a lead silicon strip sampling calorimeter, which initiates the electromagnetic showers and provides sufficient position resolution to distinguish single photons from pairs produced in neutral pion decays. The total acceptance of the barrel and endcap detectors is $|\eta| < 3.0$.

On entering the ECAL high energy electrons or photons initiate an electromagnetic shower by undergoing Bremsstrahlung or pair production respectively. The resulting cascade of particles continues to lose energy by successive Bremsstrahlung and pair production until their energy is low enough that the photons no longer undergo pair-production and the electrons lose their energy mainly by ionisation. The excitation of the

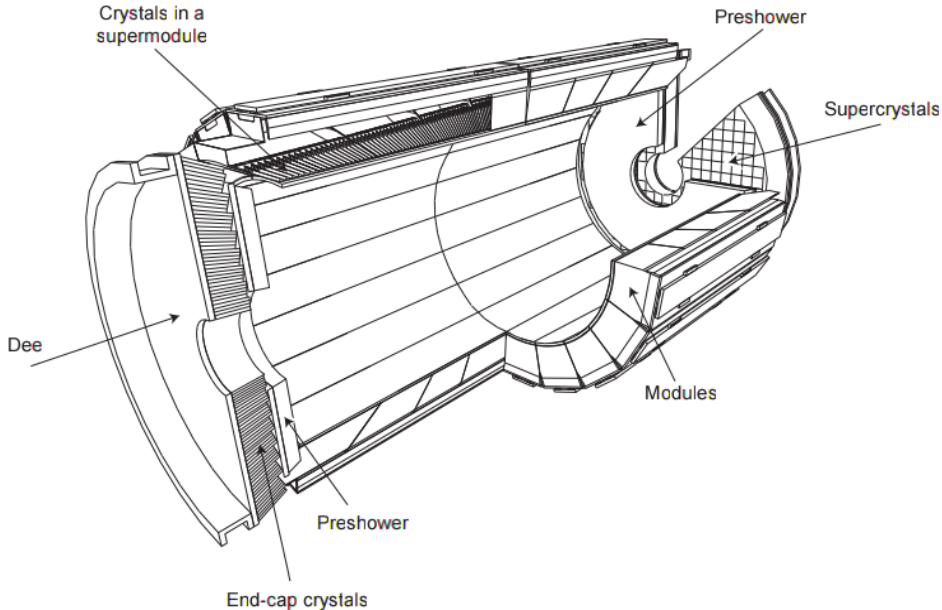


Figure 2.8: A schematic of the CMS ECAL, indicating the subsystems that comprise it. The ECAL is 7.8m long by 3.5m wide [7].

PbWO₄ crystals leads to the emission of scintillation light, proportional to the amount of energy deposited, which is collected by the photodetectors.

The choice of PbWO₄ is motivated by its high density (8.28 g/cm³), short radiation length (0.89 cm), small Moliére radius (2.2cm) and radiation hardness this leads to the showers being contained in a small area and allows the calorimeter to be compact and have fine granularity. Another advantage of PbWO₄ is that 80% of the scintillation light is emitted within the LHC's 25ns design bunch crossing time, so particles can be properly associated with the bunch crossing from which they originate.

For particle energies below 500 GeV, where the resulting shower ceases to be contained in the full depth of the ECAL, the ECAL resolution can be parametrised as:

$$\left(\frac{\sigma}{E}\right)^2 = \left(\frac{S}{\sqrt{E}}\right)^2 + \left(\frac{N}{E}\right)^2 + C^2. \quad (2.4)$$

Where S is the stochastic term, N the noise term and C the constant term. The stochastic term is comprised of fluctuations in the lateral containment of showers and also in the amount of scintillation light. The noise term is made up of electronic and digital noise, and signals from other bunch crossings which do not fully dissipate in time. The constant term comes from non-uniformity of light collection along the crystals, errors

in the calibration of crystals against each other and leakage of energy from the back of the calorimeter. The energy resolution was measured without an applied magnetic field in an electron beam using particles with momenta between 20 and 250 GeV. The stochastic, noise and constant terms were found to be $0.028 \text{ GeV}^{1/2}$, 0.12 GeV and 0.003 respectively.

As the ECAL is exposed to radiation the PbWO_4 crystals darken and as a result fewer photons are collected per unit energy deposited. The loss of response due to this darkening at the end of Run I varies from 6% for crystals in the most central region of the ECAL to 30% in the endcaps [19].

2.2.3 Hadronic calorimeter

The HCAL is designed to measure the energy of strongly interacting particles. This measurement is particularly important for neutral hadrons which do not leave tracks in the tracking system and deposit most of their energy in the HCAL, and for the determination of \cancel{E}_T . The main part of the HCAL consists of a brass and scintillator plus wavelength shifting fibre sampling calorimeter split into barrel (hadron barrel (HB)) and endcap (hadron endcaps (HE)) sections. The primary design consideration for the HCAL is that it must fit between the outer edge of the ECAL ($r = 1.77 \text{ m}$) and the inner edge of the magnet ($r = 2.95 \text{ m}$). In order to satisfy this requirement and achieve satisfactory containment of hadronic showers the magnet coil is also used as an absorber, and there is a further layer of scintillator outside the magnet coil (hadron outer (HO)). The barrel and endcap detectors extend to $|\eta| < 3$.

Brass is chosen as the main HCAL absorber because it is not magnetic and has a relatively short nuclear interaction length of 16.42 cm. Once showers have been initiated in the absorber layers they then pass through the plastic scintillator tiles, where they create pulses of light. These pulses are transferred via wavelength shifting fibres to hybrid photodiodes. The segmentation of the scintillator is such that the $\eta - \phi$ resolution in the HB (HE) is 0.087×0.087 (between 0.087×0.087 and 0.17×0.17 depending on η).

In addition to the barrel and encap sections of the HCAL there is also a steel and quartz fibre Cherenkov forward calorimeter (hadron forward (HF)), which extends the calorimetry coverage of CMS to $|\eta| < 5.2$. The choice of this technology is driven by its ability to withstand the very high particle fluxes present so close to the beamline. Showers are initiated by the steel absorber and signals are generated in the quartz fibres by particles above the Cherenkov threshold generating Cherenkov light, which is collected

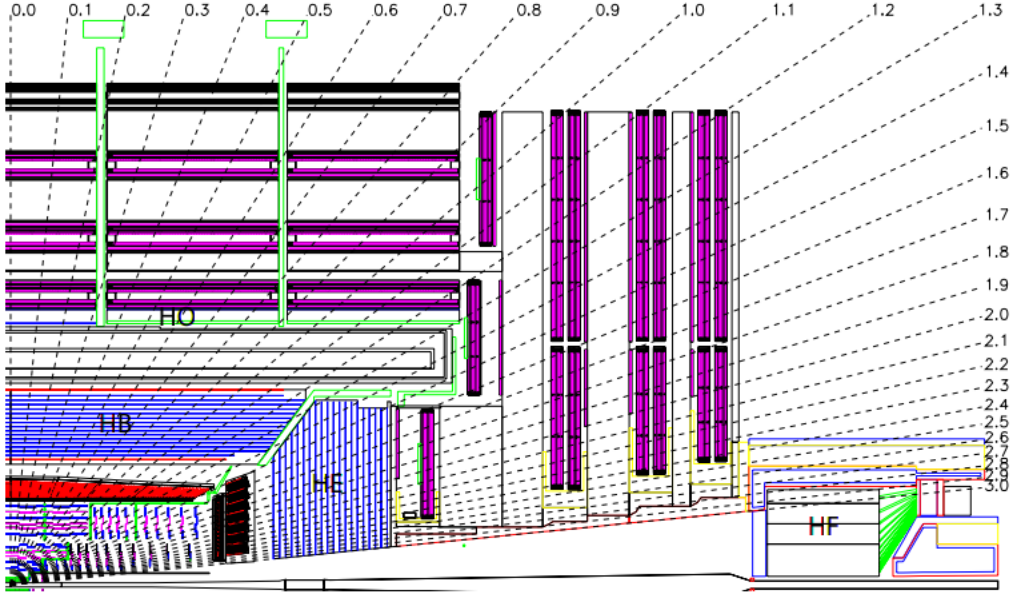


Figure 2.9: A schematic of a quadrant of the CMS HCAL in the $r - z$ plane, indicating the subsystems that comprise it [7].

by photomultiplier tubes. Due to the Cherenkov energy threshold increasing with particle mass the HF is primarily sensitive to the electromagnetic component of showers.

A diagram of the HCAL layout can be seen in Figure 2.9. In total the HCAL corresponds to 10-15 interaction lengths, depending on η . The resolution of the barrel and endcap sections of the HCAL as a function of the incident particle energy was measured in a pion beam and has been found to be well parametrised by:

$$\left(\frac{\sigma}{E}\right)^2 = \left(\frac{94.3\%}{\sqrt{E}}\right)^2 + (8.4\%)^2 \quad [20]. \quad (2.5)$$

2.2.4 Muon system

As described above muons are highly penetrating, and thus are only rarely contained by the inner detector. Very few other charged particles are able to leave the calorimeters, so the presence of tracks in the muon system is sufficient to identify muons. The muon tracking system uses three types of gaseous particle detectors, located throughout the iron magnet return yoke. In all three types of detector when a charged particle travels through the gaseous detector it ionises the gas, the resulting free electrons then drift towards the detector's anode resulting in an electrical signal. The two primary types

of detectors used are the drift tube (DT), which is used in the barrel section of the detector ($|\eta| < 1.2$), and the cathode strip chamber (CSC), which is used in the endcap ($0.9 < |\eta| < 2.4$). The DT and CSC systems identify muons and provide measurements of their momentum. These measurements can be combined with those from the tracker to improve the muon momentum resolution. This combined reconstruction and momentum measurement along with its resolution is described in Section 3.5. Additionally there is a resistive plate chamber (RPC) system in both the barrel and endcap regions ($|\eta| < 1.6$), the primary purpose of which is to provide trigger and bunch crossing identification information. A diagram of the CMS muon system can be found in Figure 2.10.

Each system has its own particular advantages and disadvantages which make it best suited for use in the various parts of the muon system. DTs are inexpensive and reliable, but they are not usable in regions with high muon and neutron background rates, making them well suited to the barrel portion of the detector, where large areas must be instrumented and rates are low. Each DT is a 2.4m long wire in a $13 \times 42\text{mm}^2$ tube. The length is limited by the segmentation of the iron return yoke, and the cross-section by the requirement that the occupancy and drift time are low enough to prevent multiple muon hits being read out at the same time. The DTs are organised in 4 stations, interspersed with return yoke iron plates. The first three stations have 8 chambers each, 4 to measure the muon's position in the $r - \phi$ plane and 4 to measure the z co-ordinate. The final outermost layer does not have the z -measuring chambers. These chambers consist of 8-12 stacked DTs, with each layer offset from the previous one by half the width of a tube to avoid gaps.

Due to their fast response time, fine segmentation and radiation resistance CSCs are ideal for the endcap region where the muon and background rates are higher. Each CSC is a multiwire proportional chamber with 7 planes of cathode strips running radially outwards with 6 planes of anode wires, which run azimuthally, interleaved between them. Both the anode and cathode wires are read out to provide η and $r - \phi$ co-ordinate measurements respectively. Similarly to the DT system the design number of CSC stations in each endcap is 4 interspersed with iron return yoke plates. During Run I only three of the CSC stations were present, the fourth station in each endcap was added during the long shutdown and is present for Run 2. The position resolution in the $r - \phi$ plane of the CSCs varies from 75-80 μm .

The RPCs are gas gaps surrounded by anode and cathode plates with read out strips between them. The advantage of RPCs is that their response is good at high rates, and they have very good time resolution, making them ideal for use in the trigger and

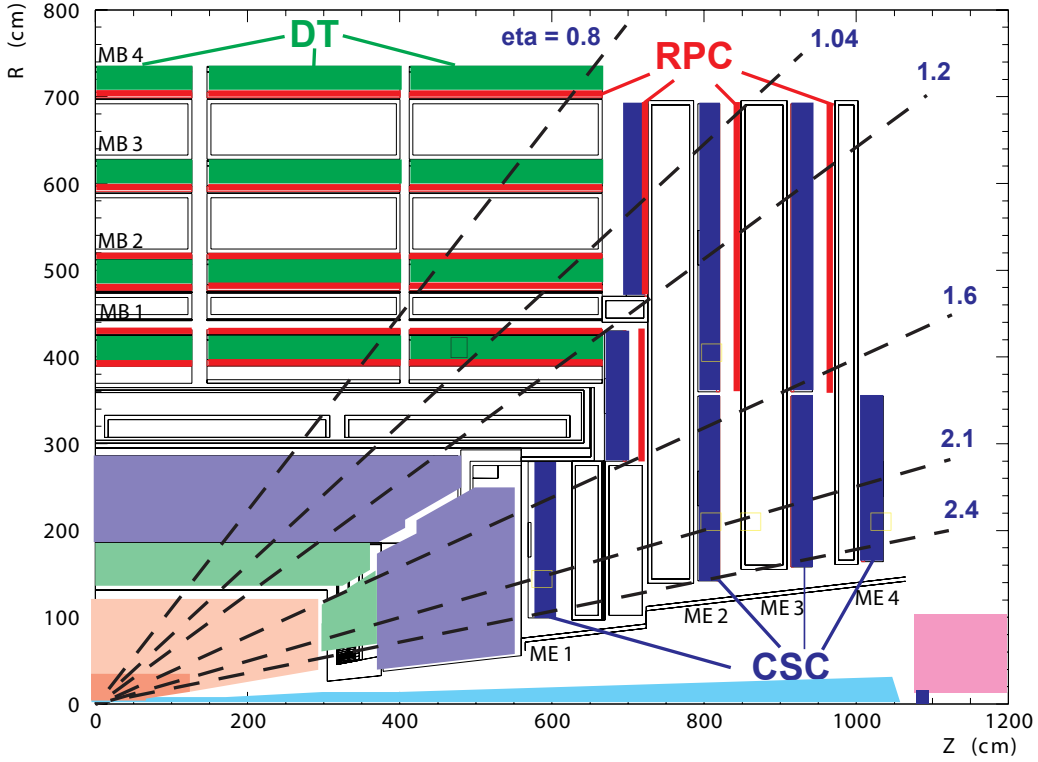


Figure 2.10: A schematic of a quadrant of the CMS muon system in the $r - z$ plane, indicating the subsystems that comprise it [21].

assignment of muons to a bunch crossing. However, they have much poorer position resolution than the DTs or CSCs. There are 6 layers of RPCs in the barrel and 3 in the endcap.

2.2.5 Trigger system and data processing

The design bunch crossing rate of the LHC is 40 MHz, and for the data used in this thesis it varied from 20-40 MHz. Since each event consists of approximately 1 MB of data, writing every event to tape would correspond to a data rate of 20-40 TB/s which is not feasible. It is also not feasible for the detector electronics to read out the detector at this frequency. It is therefore necessary to use a trigger system to reduce the event rate and select only the most interesting events.

The trigger is separated into two stages, the Level-1 (L1) trigger and the high-level trigger (HLT). First the L1 trigger, which is built of custom-designed electronics, reduces the rate to a maximum of 100 kHz. The decision to accept an event in the L1 trigger or not starts with local information on the energy deposits in the calorimeters and hits

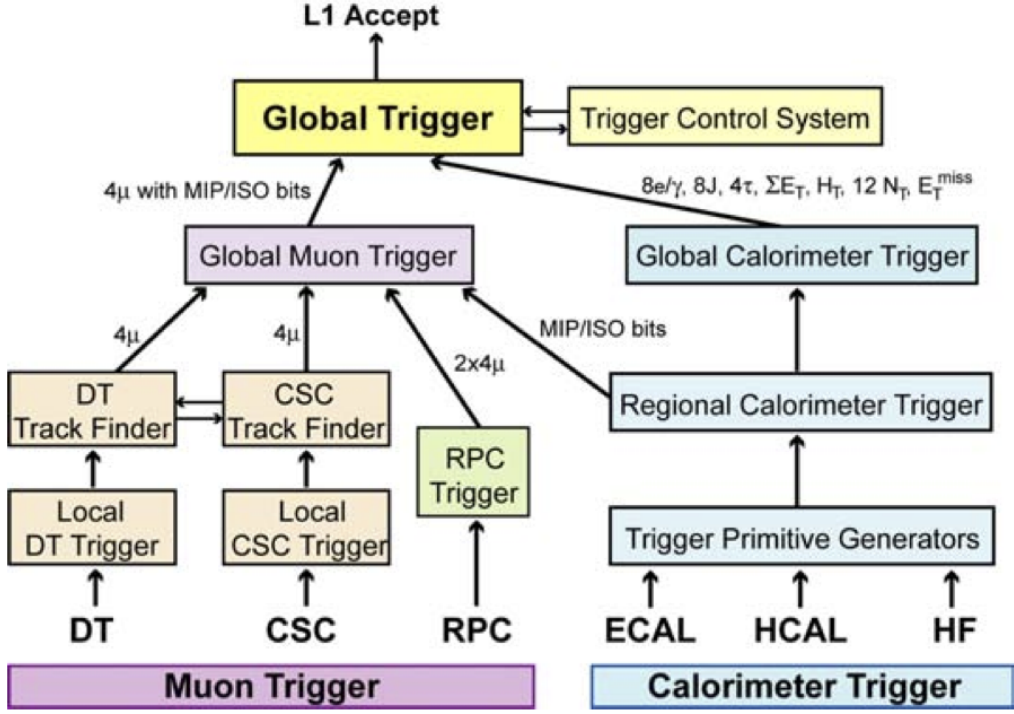


Figure 2.11: A schematic of the L1 trigger system. The arrows indicate the flow of data, the information transferred between systems is also indicated [7].

in the muon systems, which is stored for all events for 128 bunch crossings. A decision must therefore be made within 128 bunch crossings or the event is discarded. Due to the limited time available and the limited available bandwidth of the data acquisition system, this information is generally not available at the detector's full resolution. After it is collected from the detector the local information is then passed to the regional trigger systems, which generate lists of trigger candidates, such as electrons or jets, ranked by energy and quality. These ranked lists from each region are then passed to the global muon and calorimeter system triggers, which select the highest ranked candidates across the whole detector and give them to the global trigger, which makes a final decision. This process is shown in Figure 2.11.

If an event is accepted by the L1 trigger the full detector information is read out to the HLT farm on the surface, which reduces the rate further still to approximately 1 kHz. The HLT consists of several thousand commercially available CPUs. Despite having the full detector information, the time available does not allow for the full offline reconstruction to be performed. Never the less, the algorithms available at the HLT are much closer to

those used offline than those available at L1, reducing the numbers of events lost due to differences in trigger level and offline quantities.

If they are accepted by the HLT, events are sent to be reconstructed using the Worldwide LHC Computing Grid (WLCG). The WLCG consists of several tiers. Data is first fully reconstructed at the Tier 0 centres. During Run I there was only one of these at CERN, for Run II there will also be a Tier 0 centre in Budapest. It is then sent to at least one Tier 1 centre, so that a full copy of the data is available at multiple sites in different geographic locations. Tier 2 and 3 centres then process this data according to the needs of specific analyses.

During 2012 running it was found that it was possible for data to be written to tape from the CMS detector at a higher rate than it could be reconstructed by the Tier 0. 30% of the output of CMS was therefore immediately sent for “prompt” reconstruction, while the remainder was “parked” to tape to be reconstructed during LHC shutdown periods when there is spare computing capacity available [22]. The extra events that could be stored through this parking allowed significantly lower trigger selection thresholds to be used for some of the analyses described in this thesis.

Chapter 3

Physics objects and event reconstruction

This chapter describes the reconstruction of physics objects from data collected by the CMS detector. The invisible Higgs analysis uses a wide range of objects from the jets and \cancel{E}_T that are present in the signal process, to charged leptons that are present in background processes. This range of objects means that information from all subdetectors of CMS must be used. The reconstruction of each object used is described, along with the overarching “particle flow” approach to data reconstruction used by CMS.

3.1 Tracks

The tracks reconstructed in the inner tracking detector of CMS are a key part of the reconstruction of most other objects used for physics analyses. For example the jet reconstruction algorithm combines information from the tracks and calorimeter energy deposits. The algorithm used by CMS is the the Kalman filter based combinatorial track finder (CTF), which is described in [23].

The CTF starts with seeds generated from either two or three hits in the pixel tracker. In the case of seeds with two hits the nominal crossing point of the beams is used to constrain the initial momentum of the track. The initial track fit from these seeds is then improved by iterating through the layers of the tracking detector from inside to outside and updating the estimate of the track’s parameters based on the most compatible hit in each layer. After the outside of the detector is reached the algorithm checks for tracks which share more than 19% of their hits and discards the track with the fewest hits. In

the case of the two tracks having an equal number of hits the track with the best fit is kept. This process of reconstructing tracks starting from seeds is repeated up to six times, with hits associated to a successfully reconstructed track removed for the next iteration.

After the full set of iterations is complete the tracks are refitted again using a Kalman filter starting from the best fit from the innermost hits of the track and iterating outwards adding the hit associated to the track in each layer one by one. This refitting aims to reduce biases from the track’s seed including those introduced for two hit seeds that include constraints from the beamspot. The refitted tracks are then smoothed by another Kalman filter, which is initialised with the current best fit track hypothesis and iterates from the outside of the detector inwards.

The smoothed tracks then have quality criteria, such as a requirement on the maximum number of layers the track traverses without leaving a hit, imposed to reject fake tracks. The efficiency of the CTF is estimated in data using tracks from muons from Z decays, and is found to be greater than 99%.

3.2 Primary vertex

The very high instantaneous luminosities present at the LHC lead to a large probability of multiple proton-proton interactions occurring in each bunch crossing. It is therefore essential to identify the Primary Vertex (PV), which relates to the highest energy interaction or “hard scatter”. It is also useful to identify the PV to distinguish “prompt” particles directly from the hard scatter from those resulting from processes which occur later such as hadron decay or photon conversion.

The CMS PV reconstruction algorithm has three steps, track selection, clustering of tracks into vertices and finally fitting the position of these vertices and is described in more detail in [23]. In the first step, track selection, the subset of tracks with non-significant transverse impact parameters is chosen. This selection removes tracks not coming from the primary interaction region.

The next step of clustering tracks into prototype vertices uses a deterministic annealing (DA) algorithm [24]. These prototype vertices then have their best fit position determined by an adaptive vertex fitter [25], where a fit to the position of the vertex is performed, then weights, w_i are assigned to each track according to the probability that it belongs

to the vertex, before the process is repeated iteratively. Both of these algorithms also use the concept of “cooling,” where the algorithm is performed repeatedly as a parameter is gradually reduced, to increase the chance of finding the global best fit solution.

The number of degrees of freedom of the resulting vertex is defined as:

$$n_{dof} = 2 \sum_{i=1}^{\# \text{tracks}} w_i - 3. \quad (3.1)$$

This variable is highly correlated with the number of tracks compatible with the vertex and can therefore be used to select vertices coming from true proton-proton interactions.

The PV is defined to be the vertex with the highest sum of the squared p_T of all the tracks contributing to it. If there is no reconstructed vertex the nominal beam crossing point is used. In the analyses described in this thesis events are required to have a real vertex, which has $n_{dof} > 4$ and a maximum displacement in the z -direction (xy -plane) direction from the centre of the detector of 24 cm (2 cm).

The performance of the vertex reconstruction algorithm has been measured using events with at least one jet with $p_T > 20$ GeV. The efficiency to reconstruct at least one primary vertex in these events is found to be greater than 99% for vertices with at least three tracks. The position resolution is found to vary as a function of the number of tracks associated to the vertex, being approximately 100 μm for vertices with 5 tracks and approaching 10 μm for vertices with greater than 50 tracks.

3.3 Particle Flow

particle flow (PF) is an algorithm used by CMS to combine information from different sub-detectors into individual particles [26–28]. This approach is particularly beneficial for CMS as it allows the accurate momentum measurements of the inner tracker, and the excellent energy measuremetns and granularity of the ECAL to be combined and used to improve the energy measurement of objects seen in the HCAL. The PF algorithm classifies particles as charged hadrons, neutral hadrons, photons, muons and electrons. This set of particles, referred to as PF candidates, can then further be used to calculate the \cancel{E}_T , as input to the jet reconstruction, for reconstructing taus and to calculate the isolation of leptons.

The PF algorithm starts with tracks, reconstructed as described in Section 3.1, and calorimeter clusters, which are reconstructed separately in each sub-detector of the calorimeter system. Clustering starts with seeds, which are the calorimeter cells which have the local maximum energy. Cells adjacent to the cluster are added if they have energy more than twice the expected calorimeter noise. Cluster-track pairs whose cluster position and track trajectory are compatible are then linked together to identify charged particles. Linking between tracks from the inner tracker and the muon system is also performed to identify muons. The information from tracks with associated ECAL clusters, i.e. those compatible with electrons, is further used to search for clusters compatible with bremsstrahlung photons having been radiated from the track, this is described further in Section 3.4.

Once electrons, muons and charged hadrons have been identified, further calorimeter clusters are identified as neutral hadrons or photons if they are in the HCAL or ECAL respectively. Excess energy in a calorimeter cluster compared to that expected from associated tracks also allows the presence of neutral particles that would otherwise not have been identified to be determined.

3.4 Electrons

As described in Section 3.3, electrons are reconstructed by matching ECAL deposits with tracks from the inner tracker. This process is complicated by the fact that electrons can lose significant amounts of energy, in the form of bremsstrahlung photons, as they traverse the inner tracker. Approximately 35% of electrons lose at least 70% of their initial energy in this way [29]. The bremsstrahlung photons often convert to electron-positron pairs which are then further spread in the ϕ direction by CMS’s solenoidal magnetic field. The electron reconstruction, which is described in detail in reference [30], employs so-called “supercluster” algorithms to combine ECAL deposits from both the intial electron and the bremsstrahlung photons.

Due to their different geometries, different supercluster algorithms are used in the barrel and endcaps. In the barrel the “hybrid” clustering algorithm is used, this begins with seed crystals which are the crystals with local maximum energy which is greater than 1GeV. Arrays of 5×1 crystals in $\eta \times \phi$ are then added around the seed crystal if they are within 17 crystals of it in either direction in ϕ and have energy greater than 0.1GeV.

Contiguous arrays are grouped into clusters. The final supercluster consists of all clusters with energy greater than 0.35GeV.

In the endcap the “multi- 5×5 ” algorithm is used. This algorithm also starts with seed crystals, in this case those with energy higher than their four direct neighbours and also greater than 0.18 GeV. Clusters are then made up of the 5×5 square of crystals centered on the seed. Individual clusters whose seeds are within 0.07 in η and 0.3 radians in ϕ of each other are grouped and kept as a supercluster if their total energy is greater than 1GeV. A reference position for the supercluster is taken to be the energy-weighted average position of all the clusters belonging to it, and the maximum difference in ϕ between any cluster and ther reference position is taken to be the size of the cluster in ϕ . The individual clusters in a supercluster are then extrapolated to the preshower detector. Any preshower deposits within the supercluster’s ϕ size plus 0.15 radians in ϕ and within 0.15 in η of the extrapolated cluster positions are added to the supercluster.

The energy-weighted average position and energy of the final supercluster are then used to extrapolate the electron’s track back to the innermost layers of the tracker for both electron charge hypotheses. This extrapolation is then matched to hits within a wide $\phi - z$ window of it. This matched hit is used to update the estimated electron trajectory so that a hit in the second layer of the inner tracker can be searched for in a much narrower window. Hits in both the first and second layers compatible with a supercluster are then used as seeds for dedicated electron track reconstruction, performed using a Gaussian sum filter (GSF) algorithm [31], which performs better for tracks with significant energy loss.

Electron identification criteria are applied to reject fake electrons caused by other particles such as pions. The variables used include:

- $\Delta\eta_{in}$ and $\Delta\phi_{in}$, the η and ϕ distances between the electron track position extrapolated to the ECAL and the supercluster position,
- $\sigma_{i\eta i\eta}$, the energy-weighted η width of the cluster,
- H/E , the ratio between the energy deposited in the HCAL and in the ECAL in the region of the electron’s seed cluster,

all of these are generally lower for real prompt electrons.

We also require the electrons to be isolated, i.e. have a low amount of other activity present around them in the detector. The variable used for this requirement is the effective area corrected PF isolation, I_{PF} . In Run 1 (Run 2) it was defined as the sum

of the p_T of the PF candidates within a cone of $\Delta R < 0.4(0.3)$ minus the expected contribution from PU across the area of the electron.

In the vector boson fusion (VBF) invisible Higgs searches described later in this thesis two sets of requirements on the above variables are used to identify electrons. The “veto” set of identification criteria is looser and is used to veto events containing electrons. The other “tight” set of criteria is stricter and is used when it is wished to study events containing electrons. The veto (tight) criteria have an efficiency of 93% (85%) for reconstructing central electrons with $p_T > 50$ GeV [32].

3.5 Muons

Due to their relatively high mass and lack of strong force interactions, most muons deposit very little energy in the CMS calorimeters and thus leave the detector after passing through the muon system. As described in Section 3.3, this means that muons can be reconstructed by searching for compatible tracks from the inner tracker and the muon system. The approach of requiring both inner tracker and muon system tracks greatly improves the discrimination between muons and hadronic activity and is referred to as “global” muon reconstruction.

The CMS global muon reconstruction algorithm starts with each track in the muon system and searches for compatible tracks in the inner tracker [33]. If a compatible inner tracker track is found, a track fit, similar to that described in section Section 3.1, is performed using the hits in both the inner tracker and muon system. The fit accounts for energy losses as the muon traverses the detector. It is found that for muons with $p_T > 200$ GeV the global-muon fit is better than that from the tracker only. However, due to the increased hadron discrimination described above all muons used for analyses in this thesis are required to have both inner tracker and muon system tracks. As with electrons it is also required that muons are isolated. The same isolation variable, I_{PF} , as described in Section 3.4 is used for muon isolation. Global muon reconstruction is sufficient for use in vetoing events containing muons, and muons passing the above reconstruction are referred to as “veto” muons.

Where it is wished to study events containing electrons, further identification criteria are used. This is because whilst global muon reconstruction removes most hadrons, some so-called “punch through” hadrons, which are energetic enough to travel all the way through the CMS calorimeters, can still be reconstructed as muons. Furthermore, it

is desirable to separate real but non-prompt muons from hadron decay, from prompt muons from the hard scatter or tau decay. The identification consists of requiring a high quality global muon track fit, that the muon’s track passes through at least at least 5 inner tracker layers at least one being a pixel layer and that it includes at least two hits in the muon system, and that there is at least one muon system track segment present. Muons passing these additional requirements are referred to as “tight” muons.

The efficiency of veto (tight) muon reconstruction has been found to be 98-99% (96-98%) depending on the η of the muon, for muons with $p_T > 10\text{GeV}$. This efficiency measurement was performed using events with $J/\psi/PZ$ decays to muon pairs.

3.6 Jets

As it is a hadron collider quarks and gluons are very common at the LHC. Furthermore, the presence of two final state quarks is one of the primary signatures of VBF Higgs production which is one of the main focuses of this thesis. Ascertaining the momentum of these strongly interacting particles is therefore very important. As discussed in Section 1.2.2, the hadronisation of strongly interacting particles results in highly collimated jets of particles. The momentum of the original parton which gave rise to the jet can be reconstructed by combining all of the particles in the resulting jet.

3.6.1 Jet clustering

Jet clustering algorithms take the many different types of particles that are expected to be present in the particle showers from hadronisation, and combine them into jets [34]. It is important that jet clustering algorithms do not produce different reconstructed jets if a jet undergoes soft QCD radiation (called infrared unsafety) or if a gluon in it splits in two (called colinear unsafety). The algorithm used by CMS is a so-called sequential recombination algorithm. This class of algorithms requires a metric for calculating the distance between particles in the event, d_{ij} , and a metric for calculating the distance to a nominal beamline particle, d_{iB} to be defined. The algorithms then proceed as follows:

- 1 Calculate the distance between all pairs of particles in the event including the nominal beamline,

- 2 If the smallest distance is a d_{ij} combine i and j together into a single new particle and return to step 1.
- 3 If the smallest distance is a d_{iB} , consider i to be a final state jet and remove it from the list of particles. Return to step 1.
- 4 Stop when no particles remain.

The particular algorithm used by CMS is the infrared and colinear safe anti- k_T algorithm, its distances are defined as:

$$d_{ij} = \min(p_{Ti}^{-2}, p_{Tj}^{-2}) \frac{\Delta R_{ij}^2}{R^2}, \quad (3.2)$$

$$d_{iB} = p_{Ti}^{-2}, \quad (3.3)$$

where ΔR_{ij} is the distance in the $\eta - \phi$ plane between particles i and j and R is a parameter of the algorithm analogous to the maximum radius of the jet. This algorithm starts by clustering around the hardest particle in a region and therefore usually produces circular jets, with easy to calculate areas.

The anti- k_T algorithm is implemented using the FASTJET package with the PF candidates, described in Section 3.3, used as input [35]. For analyses using data from LHC Run 1 (Run 2) R of 0.5 (0.4) is used.

3.6.2 Jet identification

In order to reject jets that are badly reconstructed or just due to detector noise, identification criteria are imposed on the jets reconstructed by the above algorithm. These requirements are that:

- The jet contains at least two PF candidates.
- The total jet energy contribution from neutral hadrons must be less than 99% as must that from photons.
- The jet has contributions from both the ECAL and HCAL.
- Jets with η such that tracking information is available must have at least one charged object which contributes to the jet's energy and less than 99% of their energy from electrons.

Real jets pass these requirements with over 99% efficiency [36].

In addition to jets from detector noise, it is also possible for the jet reconstruction to include particles that are not from the PV, but instead come from PU vertices. This can lead either to an overestimation of the energy of a real jet from the PV, or to fake jets made up of energy from several vertices. The CMS pileup jet identification procedure [37] combines several variables sensitive to the pileup contribution in a jet, such as information on how the p_T of the jet is shared between its constituents and the constituents tracking information, into a boosted decision tree (BDT) [38]. Simulated real jets from quarks pass this identification with 88-99% efficiency depending on how central they are, while jets from pile-up are rejected with 40-87% efficiency.

Finally, jets which are within 0.5 in the $\eta - \phi$ plane of any veto electron, defined in Section 3.4 or veto muon, defined in Section 3.5 are vetoed, to avoid using jets which are due to misreconstructed leptons.

3.6.3 Jet energy corrections

The energy of the jets clustered and identified by the CMS jet reconstruction often does not match the energy of the particle that initiated the jet. This can have many causes such as additional energy from PU, miscalibration of the energy response of the calorimeters or energy deposited in uninstrumented areas of the detector. To correct for these mismatches a correction to the jet energy is applied that has the following functional form and is described in detail in reference [39]:

$$p_\mu^{\text{cor}} = C_{\text{offset}}(p_T^{\text{raw}}) \cdot C_{\text{rel}}(\eta) \cdot C_{\text{abs}}(p'_T) \cdot C_{\text{res}}(p''_T, \eta) \cdot p_\mu^{\text{raw}}. \quad (3.4)$$

Each C in the equation represents a correction, p_μ^{cor} is the corrected jet four-momentum, p_μ^{raw} is the jet four-momentum before correction, p'_T is the p_T after the offset and relative correction, C_{offset} and p''_T is the p_T after all but the residual correction, C_{abs} .

The purpose of C_{offset} is to remove energy from the jet which is not due to activity from the PV such as detector noise and PU. The correction is calculated on a jet-by-jet basis by multiplying the median p_T density of the event the jet is in by the jet's area.

The relative correction, C_{rel} , serves to make the jet energy response uniform in η . Monte Carlo (MC) truth information and the dijet p_T balance method, where the p_T of a well measured jet in the central region of the detector is compared to a second jet at a different η in events with only two jets, in data are used to calculate C_{rel} .

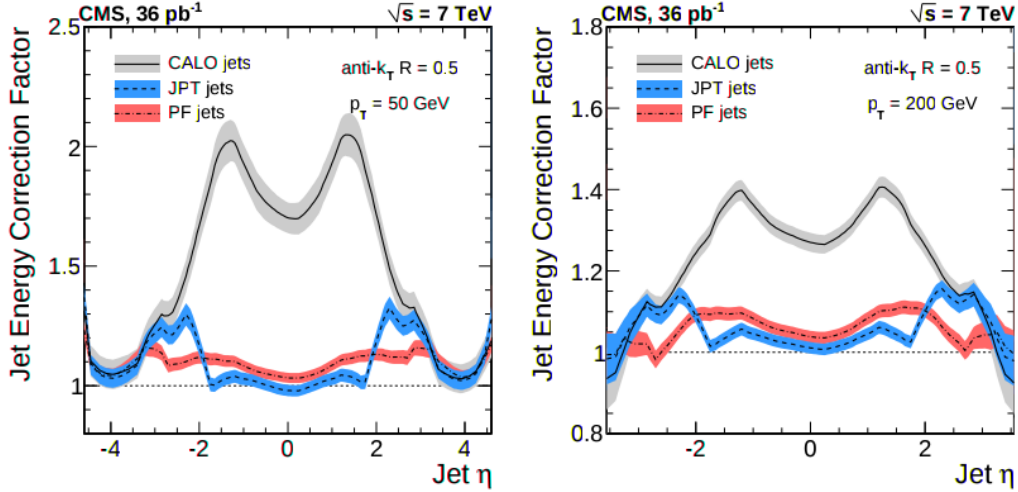


Figure 3.1: Total jet-energy-correction factor as a function of jet η for jets with $p_T = 50\text{GeV}$ (left) and $p_T = 200\text{GeV}$ (right), for several types of jet reconstruction used at CMS. The bands indicate the corresponding uncertainty [39].

The absolute correction C_{abs} , makes the jet energy response uniform in p_T . The correction is calculated in MC with MC truth information and in data by using $Z/\gamma + \text{jets}$ events, where the transverse momentum of the jets should balance the Z/γ . Both Z bosons which decay leptonically and photons have very good energy resolution, so any imbalances can be assumed to be due to jet mismeasurement, and a correction calculated.

Finally C_{res} , which is applied only to data and not MC, corrects for residual differences seen in both p_T and η response between data and MC. The total uncertainty on the overall jet energy correction is taken to be the sum in quadrature of the uncertainties on the individual corrections. The correction and its uncertainty are shown in Figure 3.1, the other two types of jets in the figure are not used in analyses described in this thesis and so are not discussed.

3.7 Missing transverse energy

Particles which interact only weakly with normal matter such as neutrinos and hypothetical DM particles will pass through the CMS detector without interacting. The only signature that they leave is a momentum imbalance between the visible particles in an event. The high hermeticity of the CMS detector allows this imbalance, referred to as \cancel{E}_T , to be measured accurately. As the analyses described in this thesis are searches for invisibly decaying Higgs bosons, the measurement of \cancel{E}_T is crucial.

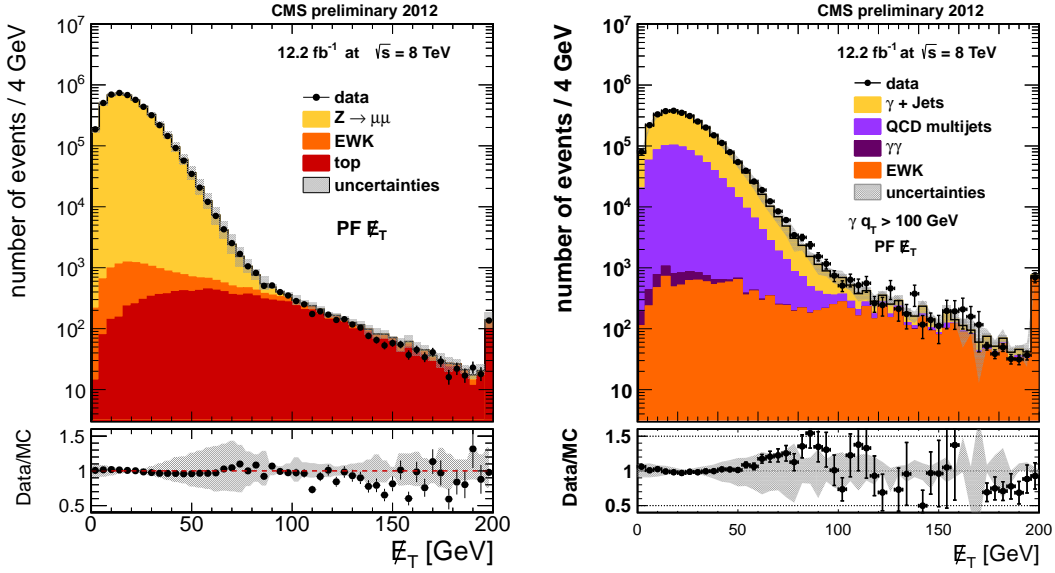


Figure 3.2: Distributions of the uncorrected \cancel{E}_T in $Z \rightarrow \mu\mu$ events (left) and $\gamma + \text{jets}$ events (right) in $\sqrt{s} = 8$ TeV data and simulation. The shaded band corresponds to the systematic uncertainty [40].

The CMS \cancel{E}_T reconstruction algorithm defines the \cancel{E}_T as the negative vectorial sum of the p_T of all PF candidates [40]. For processes such as Z boson decays to muon pairs or $\gamma + \text{jets}$ there should be no \cancel{E}_T as all the decay products are visible. However, as can be seen from Figure 3.2, these events often still appear to have \cancel{E}_T due to resolution of the p_T measurements of the various objects making up the PF candidates, primarily the jets which are numerous and do not have as good resolution as other objects.

The jet energy corrections, described in Section 3.6.3, alter the energy of jets, and in doing so alter the total energy present in the event, these changes are propagated to the \cancel{E}_T . Furthermore, as charged particle flow candidates can be determined to be from the PV or a PU vertex it is also possible to correct the \cancel{E}_T for PU contributions. This correction uses the ratio of the energy response of CMS for charged and neutral particles to calculate the neutral PU contribution can be estimated from the charged PU contribution.

In addition to the above corrections filters are applied to reject events where detector or beam effects lead to a high probability of spurious \cancel{E}_T . Examples of the effects which are removed with these filters include particles directly hitting the photodetectors in the ECAL or significant energy deposits from the halo of particles surrounding the LHC beam.

In the VBF invisible Higgs boson decay searches described below events with Z boson decays to muons are used to estimate the rate of Z boson decays to neutrinos. As part of this estimation the muons from the Z boson decay are ignored when calculating the \cancel{E}_T , the resulting variable is referred to as $\cancel{E}_T^{\text{no-}\mu}$.

3.8 Taus

Chapter 4

Methods for limit setting

Chapter 5

Search for invisibly decaying Higgs bosons in Run 1 prompt data

5.1 Trigger and event selection

5.2 Background estimation

5.2.1 $W \rightarrow e\nu + \text{jets}$

5.2.2 $W \rightarrow \mu\nu + \text{jets}$

5.2.3 $W \rightarrow \tau\nu + \text{jets}$

5.2.4 $Z \rightarrow \nu\nu + \text{jets}$

5.2.5 QCD

5.2.6 Minor backgrounds

5.3 Systematic uncertainties

5.4 Results

Chapter 6

Search for invisibly decaying Higgs bosons in Run 1 parked data

6.1 Trigger

6.2 Event selection

6.3 Background estimation

6.3.1 $W \rightarrow e\nu + \text{jets}$

6.3.2 $W \rightarrow \mu\nu + \text{jets}$

6.3.3 $W \rightarrow \tau\nu + \text{jets}$

6.3.4 $Z \rightarrow \nu\nu + \text{jets}$

6.3.5 QCD

6.3.6 Minor backgrounds

6.4 Systematic uncertainties

6.5 Results

Chapter 7

Combinations and interpretations of Run 1 searches for invisibly decaying Higgs bosons

7.1 Searches in other channels

7.2 Combination with prompt VBF search

7.3 Combination with the parked VBF search

7.4 Dark matter interpretations

Chapter 8

Search for invisibly decaying Higgs bosons in Run 2 data

Bibliography

- [1] D. Hanneke, S. Fogwell, and G. Gabrielse, “New Measurement of the Electron Magnetic Moment and the Fine Structure Constant”, *Phys. Rev. Lett.* **100** (Mar, 2008) 120801, [doi:10.1103/PhysRevLett.100.120801](https://doi.org/10.1103/PhysRevLett.100.120801).
- [2] E. Noether, “Invariant Variation Problems”, *Gott. Nachr.* **1918** (1918) 235–257, [doi:10.1080/00411457108231446](https://doi.org/10.1080/00411457108231446), [arXiv:physics/0503066](https://arxiv.org/abs/physics/0503066). [Transp. Theory Statist. Phys.1,186(1971)].
- [3] E. Noether, “Invariant variation problems”, *Transport Theory and Statistical Physics* **1** (1971), no. 3, 186–207, [doi:10.1080/00411457108231446](https://doi.org/10.1080/00411457108231446).
- [4] C. N. Yang and R. L. Mills, “Conservation of Isotopic Spin and Isotopic Gauge Invariance”, *Phys. Rev.* **96** (Oct, 1954) 191–195, [doi:10.1103/PhysRev.96.191](https://doi.org/10.1103/PhysRev.96.191).
- [5] Particle Data Group Collaboration, “Review of Particle Physics”, *Chin. Phys. C* **38** (2014) 090001, [doi:10.1088/1674-1137/38/9/090001](https://doi.org/10.1088/1674-1137/38/9/090001).
- [6] D. Griffiths, “Introduction to Elementary Particles”. Physics textbook. Wiley, 2008.
- [7] C. Collaboration, “The CMS experiment at the CERN LHC”, *JINST* **3** (2008) S08004, [doi:10.1088/1748-0221/3/08/S08004](https://doi.org/10.1088/1748-0221/3/08/S08004).
- [8] L. Evans and P. Bryant, “LHC Machine”, *JINST* **3** (2008), no. 08, S08001, [doi:10.1088/1748-0221/3/08/S08001](https://doi.org/10.1088/1748-0221/3/08/S08001).
- [9] LEP Injector Study Group, “LEP design report, volume I: The LEP injector chain; LEP design report, volume II: The LEP Main Ring”. CERN, Geneva, 1983.
- [10] A. Collaboration, “The ALICE experiment at the CERN LHC”, *JINST* **3** (2008) S08002, [doi:10.1088/1748-0221/3/08/S08002](https://doi.org/10.1088/1748-0221/3/08/S08002).
- [11] A. Collaboration, “The ATLAS Experiment at the CERN Large Hadron Collider”, *JINST* **3** (2008) S08003, [doi:10.1088/1748-0221/3/08/S08003](https://doi.org/10.1088/1748-0221/3/08/S08003).

- [12] LHCb Collaboration, “The LHCb Detector at the LHC”, *JINST* **3** (2008) S08005, [doi:10.1088/1748-0221/3/08/S08005](https://doi.org/10.1088/1748-0221/3/08/S08005).
- [13] M. Benedikt, P. Collier, V. Mertens et al., “LHC Design Report”. CERN, Geneva, 2004.
- [14] CMS Collaboration, “CMS Luminosity - Public Results”,.
- [15] W. J. Stirling, “Private communication”,.
- [16] T. Sakuma and T. McCauley, “Detector and Event Visualization with SketchUp at the CMS Experiment”, *J. Phys.: Conf. Ser.* **513** 022032, [doi:10.1088/1742-6596/513/2/022032](https://doi.org/10.1088/1742-6596/513/2/022032).
- [17] CMS Collaboration, “Interactive Slice of the CMS detector”, *CMS Document 4172-v2*.
- [18] Tricomi, Alessia, “Performances of the ATLAS and CMS silicon tracker”, *Eur Phys J C* **33** (2004) s1023–s1025, [doi:10.1140/epjcd/s2004-03-1801-1](https://doi.org/10.1140/epjcd/s2004-03-1801-1).
- [19] CMS Collaboration Collaboration, “History of ECAL response with laser data”,.
- [20] USCMS, ECAL/HCAL Collaboration, “The CMS barrel calorimeter response to particle beams from 2-GeV/c to 350-GeV/c”, *Eur. Phys. J.* **C60** (2009) 359–373, [doi:10.1140/epjc/s10052-009-0959-5](https://doi.org/10.1140/epjc/s10052-009-0959-5), [10.1140/epjc/s10052-009-1024-0](https://doi.org/10.1140/epjc/s10052-009-1024-0).
[Erratum: *Eur. Phys. J.C*61,353(2009)].
- [21] CMS Collaboration Collaboration, “CMS Physics: Technical Design Report Volume 1: Detector Performance and Software”. Technical Design Report CMS. CERN, Geneva, 2006. There is an error on cover due to a technical problem for some items.
- [22] CMS Collaboration Collaboration, “Data Parking and Data Scouting at the CMS Experiment”,.
- [23] T. C. Collaboration, “Description and performance of track and primary-vertex reconstruction with the CMS tracker”, *Journal of Instrumentation* **9** (2014), no. 10, P10009.
- [24] K. Rose, “Deterministic Annealing for Clustering, Compression, Classification, Regression, and related Optimization Problems”, *Proceedings of the IEEE* **86** (1998) 2210.
- [25] R. Fruhwirth, W. Waltenberger, and P. Vanlaer, “Adaptive vertex fitting”, *J. Phys. G* **34** (2007) N343, [doi:10.1088/0954-3899/34/12/N01](https://doi.org/10.1088/0954-3899/34/12/N01).

- [26] CMS Collaboration, “Particle-Flow Event Reconstruction in CMS and Performance for Jets, Taus, and MET”, *CMS Physics Analysis Summary CMS-PAS-PFT-09-001* (2009).
- [27] CMS Collaboration, “Commissioning of the Particle-flow Event Reconstruction with the first LHC collisions recorded in the CMS detector”, *CMS Physics Analysis Summary CMS-PAS-PFT-10-001* (2010).
- [28] CMS Collaboration, “Commissioning of the Particle-Flow reconstruction in Minimum-Bias and Jet Events from pp Collisions at 7 TeV”, *CMS Physics Analysis Summary CMS-PAS-PFT-10-002* (2010).
- [29] S. Baffioni, C. Charlot, F. Ferri et al., “Electron reconstruction in CMS”, *Eur. Phys. J.* **C49** (2007) 1099–1116, [doi:10.1140/epjc/s10052-006-0175-5](https://doi.org/10.1140/epjc/s10052-006-0175-5).
- [30] C. collaboration, “Performance of electron reconstruction and selection with the CMS detector in proton-proton collisions at $s=8\text{TeV}$ ”, *Journal of Instrumentation* **10** (2015), no. 06, P06005.
- [31] W. Adam, R. Frühwirth, A. Strandlie et al., “Reconstruction of Electrons with the Gaussian-Sum Filter in the CMS Tracker at the LHC”, *CMS Note CMS-NOTE-2005-001* (2005).
- [32] L. Sani, “Private communication”,.
- [33] CMS Collaboration, “Performance of CMS muon reconstruction in pp collision events at $\sqrt{s} = 7 \text{ TeV}$ ”, *JINST* **7** (2012) P10002, [doi:10.1088/1748-0221/7/10/P10002](https://doi.org/10.1088/1748-0221/7/10/P10002), [arXiv:1206.4071](https://arxiv.org/abs/1206.4071).
- [34] G. P. Salam, “Towards Jetography”, *Eur. Phys. J.* **C67** (2010) 637–686, [doi:10.1140/epjc/s10052-010-1314-6](https://doi.org/10.1140/epjc/s10052-010-1314-6), [arXiv:0906.1833](https://arxiv.org/abs/0906.1833).
- [35] M. Cacciari, G. P. Salam, and G. Soyez, “FastJet User Manual”, *Eur. Phys. J. C* **72** (2012) 1896, [doi:10.1140/epjc/s10052-012-1896-2](https://doi.org/10.1140/epjc/s10052-012-1896-2), [arXiv:1111.6097](https://arxiv.org/abs/1111.6097).
- [36] N. Saoulidou and E. Tziaferi, “Performance of the Particle-Flow jet identification criteria using proton-proton collisions at 8 TeV”, *CMS Analysis Note: AN-14-227* (2014).
- [37] CMS Collaboration, “Pileup Jet Identification”, *CMS Physics Analysis Summary CMS-PAS-JME-13-005* (2013).

- [38] A. Hocker, J. Stelzer, F. Tegenfeldt et al., “TMVA - Toolkit for Multivariate Data Analysis”, *PoS ACAT* (2007) 040, [arXiv:physics/0703039](https://arxiv.org/abs/physics/0703039).
- [39] CMS Collaboration, “Determination of jet energy calibration and transverse momentum resolution in CMS”, *JINST* **6** (2011) 11002,
[doi:10.1088/1748-0221/6/11/P11002](https://doi.org/10.1088/1748-0221/6/11/P11002), [arXiv:1107.4277](https://arxiv.org/abs/1107.4277).
- [40] CMS Collaboration, “Performance of Missing Transverse Momentum Reconstruction Algorithms in Proton-Proton Collisions at $\sqrt{s} = 8$ TeV with the CMS Detector”, *CMS Physics Analysis Summary CMS-PAS-JME-12-002* (2013).

List of figures

2.1	The layout of the chain of accelerators feeding into the LHC, showing the position of the four main detectors.	11
2.2	A summary of the luminosity delivered to CMS during Run 1 of the LHC[14].	13
2.3	Cross-sections for several processes in collisions of protons with protons or anti-protons as a function of centre of mass energy. The energies that the LHC and Tevatron ran at are highlighted[15].	14
2.4	Distribution of the number of interactions per bunch crossing in CMS during 2012 running of the LHC[14].	15
2.5	A diagram of the subsystems making up the CMS detector, illustrating the hermeticity and layered structure of the experiment[16].	16
2.6	A schematic cross-section of the CMS experiment showing the path taken by several types of particles[17].	17
2.7	A cross-section of the CMS tracker, indicating the subsystems that comprise it. Each line indicates a detector module[7].	18
2.8	A schematic of the CMS ECAL, indicating the subsystems that comprise it. The ECAL is 7.8m long by 3.5m wide[7].	20
2.9	A schematic of a quadrant of the CMS HCAL in the $r - z$ plane, indicating the subsystems that comprise it[7].	22
2.10	A schematic of a quadrant of the CMS muon system in the $r - z$ plane, indicating the subsystems that comprise it[21].	24
2.11	A schematic of the L1 trigger system. The arrows indicate the flow of data, the information transferred between systems is also indicated[7]. . .	25
3.1	Total jet-energy-correction factor as a function of jet η for jets with $p_T = 50\text{GeV}$ (left) and $p_T = 200\text{GeV}$ (right), for several types of jet reconstruction used at CMS. The bands indicate the corresponding uncertainty[39].	36
3.2	Distributions of the uncorrected \cancel{E}_T in $Z \rightarrow \mu\mu$ events (left) and $\gamma + \text{jets}$ events (right) in $\sqrt{s} = 8\text{TeV}$ data and simulation. The shaded band corresponds to the systematic uncertainty[40].	37

List of tables

1.1	The fundamental fermions observed in nature separated into their three generations. Each particle shown also has an antiparticle with opposite charge and identical mass. Values taken from[5]	3
1.2	The fundamental vector bosons observed in nature separated by the force which they mediate. Values taken from[5].	4

List of Acronyms

VBF vector boson fusion

DM dark matter

PSB Proton Synchrotron Booster

PS Proton Synchrotron

SPS Super Proton Synchrotron

PU pile-up

SM standard model

BSM beyond the SM

QFT quantum field theory

ECAL electromagnetic calorimeter

HCAL hadron calorimeter

EB ECAL barrel

EE ECAL endcap

HB hadron barrel

HE hadron endcaps

HF hadron forward

HO hadron outer

L1 Level-1

HLT high-level trigger

CSC cathode strip chamber

DT drift tube

RPC resistive plate chamber

PV Primary Vertex

CTF combinatorial track finder

DA deterministic annealing

PF particle flow

GSF Gaussian sum filter

BDT boosted decision tree

MC Monte Carlo

WLCG Worldwide LHC Computing Grid